Serdar Hicdurmaz
German Aerospace Center (DLR),
Institute of Solar Research,
Stuttgart 70569, Germany,
e-mail: serdar.hicdurmaz@dlr.de

Reiner Buck
German Aerospace Center (DLR),
Institute of Solar Research,
Stuttgart 70569, Germany,
e-mail: reiner.buck@dlr.de

Bernhard Hoffschmidt
German Aerospace Center (DLR),
Institute of Solar Research,
Cologne 51147, Germany,
e-mail: bernhard.hoffschmidt@dlr.de

Image Analysis of Particle Flow in Centrifugal Solar Particle Receiver

Particle solar receivers promise economical and operational advantages compared to the molten salt-based solar receivers. In this study, an experiment is designed to observe the particle flow characteristics in the Centrifugal Particle Solar Receiver. A set of experiments for various receiver rotational speeds and particle mass flowrates is conducted, and experimentally obtained raw results are post-processed by means of an Image Processing Routine based on 4BestEstimate algorithm. The axial advance of the particles in one receiver rotation, the particle film thickness, and the ratio of the length of the stationary zone to the receiver circumference is measured to be later used in the validation study of the discrete element method-based numerical model. [DOI: 10.1115/1.4053464]

Keywords: solar particle receiver, lagrangian particle tracking, image processing, concentrating solar power, solar tower

1 Introduction

Solar towers using sand-like granular particles as heat transfer fluid (HTF) have various advantages over the molten salt-based solar receivers, which are the state-of-the-art concentrating solar tower technology. Particle-based systems can operate at higher temperatures; thus, the solar-to-electricity efficiency is improved. Moreover, they promise higher storage density and lower expected operational and component costs compared to molten-salt based systems [1]. The Centrifugal Solar Particle Receiver (CentRec) is a promising design when compared with other particle receiver concepts in terms of the particle residence time adjustability. In this receiver type, the ceramic particles that are accelerated centrifugally and gravitationally descend through the inclined rotating receiver and form a thin particle film layer while being directly exposed to the solar radiation through the aperture (Fig. 1(*b*)). Wu [2] demonstrated that an opaque particle film can be obtained for various receiver rotational speeds and particle mass flowrates by employing a proof-of-concept scale receiver with 17 cm cavity diameter. Later, the same size receiver is tested in high flux solar simulator, and 75% efficiency is obtained for a mean flux of 670 kW/m^2 at a aperture plane [3]. Ebert et al. [4] scaled up the design to 1 m^2 of aperture area and tested the stability of the particle film. However, for further economical and thermal optimization of the CentRec design, the particle film thickness should be optimized to eliminate the risk of the high temperature gradients in the radial direction within the particle film and the risk of excessive heating the receiver wall while the receiver operates at full load. In modeling of the solar particle receivers, discrete element method (DEM)-based numerical models that consider the solid particles as a discrete phase and solve equations of motion individually for each one to predict their trajectories has been developed in recent years [5,6]. However, DEM particle properties like the particle sliding friction and the rolling friction, accounting for the surface roughness and non-spherical nature of particles, respectively, must be calibrated in advance. Grobbel et al. [7] calibrated DEM particle properties for the ceramic particles being candidate for concentrating solar power applications by using the bulk calibration approach. However, a receiver scale comparison of the numerical and the experiment results, which assesses how accurately the DEM model predicts the dynamics of the particle film in CentRec, has to be carried out in order to check the applicability of DEM particle property calibration study results to the numerical CentRec model. In this work, a set of experiments of which results will be used in the validation of the numerical model is addressed.

In CentRec, particles are introduced at the top of the rotating receiver by means of the particle distributor, and thanks to the centrifugal effects, form a thin layer on the wall (Fig. 1). Due to the superposition of centrifugal and gravity effects, the particles either descend in the axial (receiver centerline) direction or remain stationary relative to the rotating receiver [8]. Depending on the receiver rotational speed and the receiver inclination angle, two distinct zones, called as a stationary and a moving zone according to observer on the ground are observed while the receiver rotates. Particles are stationary at the bottom part of the receiver circumference where gravity and centrifugal force are in the same direction. On the other hand, they move in axial direction at the top part of receiver circumference where forces tend to counterbalance each other. The magnitude and direction of the net force acting on particle film affect the friction force acting on bulk. A more detailed discussion about movement of particles can be found in authors' previous work [8].

In this study, an optical system consisting of diffusively radiating lamps and GoPro® cameras, shown in Fig. 2, is integrated to the lab scale CentRec, shown in Fig. 1, to determine the particle flow characteristics. Although 2D feature tracking-like approaches are used in the measurement of particle velocity in other solar particle receiver concepts [9], the common approaches to track the motion of moving granular particles are particle image velocimetry (PIV) and particle tracking velocimetry (PTV) [10,11]. In PIV, the velocity field of a group of particles in a region of interest is measured by assuming that the particle phase is a continuum. However, in PTV, the discrete motion of individual particles is tracked. Unlike this study, where tracer particles move in particulate medium, in most PIV studies, tracer particles are injected to the gaseous or liquid medium and tracked with high-speed cameras to investigate the flow behavior of moving fluid [12,13]. Although PIV systems give accurate results in dense flow regimes, PTV technique is advantageous in dilute systems because it tracks each individual particle and provides more detailed information about individual particle motion. In this study, PTV is preferred because DEM-based simulation can also calculate particle trajectories; thus, a particle scale comparison can be done. Gollin et al [14] stated that PTV

Contributed by the Solar Energy Division of ASME for publication in the Journal of Solar Energy Engineering: Including Wind Energy and Building Energy Conservation. Manuscript received August 20, 2021; final manuscript received November 25, 2021; published online January 31, 2022. Assoc. Editor: Nesrin Ozalp.

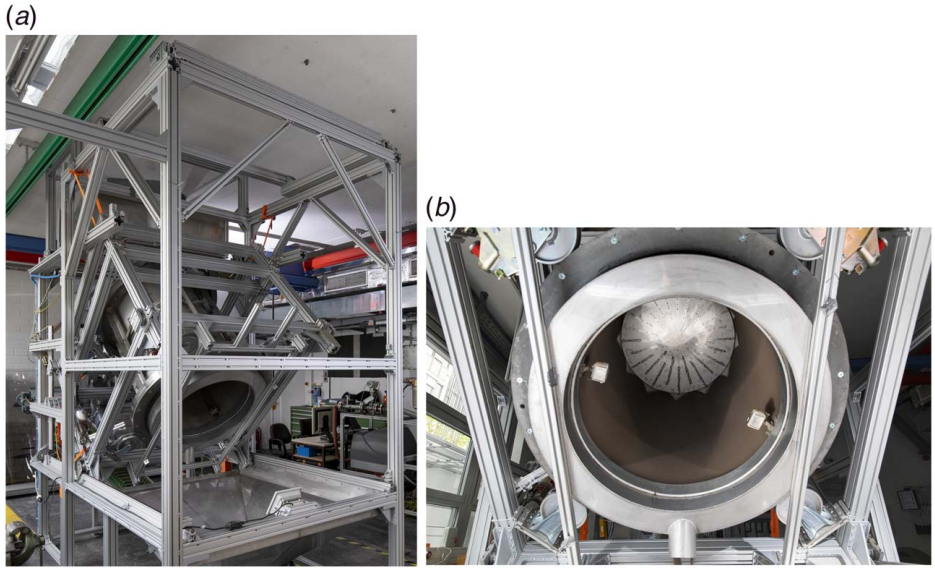

Fig. 1 (*a*) Centrifugal Solar Particle Receiver and (*b*) particle film descending through rotating receiver wall

technique suffers from two difficulties. The first is the accurate determination of the particle position and the second is the linear approximation of the particle trajectory between measured particle positions. To accurately determine the particles' position requires the calibration of the camera to eliminate the optical distortion such as fisheye effect [15,16]. Later, a 2D image of tracers moving in a particle bulk is obtained for each camera frame. However, it is very likely that the whole periphery of the tracer is not distinguishable due to eclipsing of neighboring particles. Liebl [17] developed a deterministic approach to decide whether the detected pixel group constitute a traced particle (tracer) or not. In this study, this deterministic approach is tailored for CentRec application. After finding the tracers' position in 2D images, a tracking algorithm connecting these positions in sequential frames is needed. Ouellette et al. [18] developed a particle tracking algorithm, called 4BestEstimate, based on the theory that the tracer's position in the current frame can be best estimated by using the previous two frames and one following frame. Although the trajectory of a particle is assumed as linear between two consecutive frames, this assumption does not cause a large error for CentRec application because the axial displacement of a tracer in one full rotation of the receiver is considered as the validation parameter instead of using the full trajectory of tracers. In addition to this, the film thickness and the ratio of the length of the stationary part, i.e., the length of the arc where particles' axial velocity is zero, to the receiver circumference are also measured for various rotational speeds and mass flowrates. Later, these parameters will be used in the validation of the numerical model.

Fig. 2 The Optical Elements: ① The Ring Light, ② The Camera for the particle tracking, ③ The camera for the film thickness, ④ The bar light, and ⑤ The circular pin

2 Experiment Setup

2.1 Centrec Setup. In the experiment, a closed loop particle circulation system is employed. The particles leaving the receiver are transported to the storage tank via a conveyor belt and a bucket elevator, respectively. Then, the hopper located above the receiver is filled with the particles from the storage tank. The receiver cavity diameter is 80 cm, whereas the axial length is 120 cm. The receiver inclination angle is set to 45 deg. In this study, a passive particle feeding system is utilized by means of an orifice plate. Orifice plates with a hole diameter of 16, 22.5, 25, and 30 mm are calibrated, and the corresponding mass flowrates are found as 0.092, 0.238, 0.312, and 0.489 kg/s, respectively [19]. In order to be able to track the particle motion, ZrO_2-based white tracer particles are mixed with the reddish-brown ceramic particles. The weight ratio of the tracers to the particles is 0.01. While the mean sieve diameters of the tracers and the particles are 0.983 mm and 0.967 mm, respectively, the static angle of reposes are found as 22.14 deg and 27.02 deg because the tracers are more spherical [17]. The ceramic particles are SG 16/30 type provided by Saint Gobain®, and their size distribution can be found

Table 1 Experiment parameters

	Parameter	Unit	Value
Fixed Parameters	Cavity diameter	m	0.8
	Cavity length	m	1.2
	Receiver inclination	degree	45
	Diameter of wire welded to cavity wall	mm	1
	Size of rectangular mesh formed by wires	mm	2 × 2
	Ceramic particle mean sieve diameter	mm	0.983
	Tracer particle mean sieve diameter	mm	0.967
	Tracer to particle ratio	–	0.01
	Cropped image dimension	mm	136.56 (hor.) × 72.83 (ver.)
	Pixel edge length	mm	0.07586
Independent (Operational) Parameters	Receiver rotational speed	rpm	62, 63, 64, 65, 66, 67
	Particle mass flowrate	kg/s	0.092, 0.238, 0.312, 0.489
Dependent Parameters	Tracers' axial advance in 1 rotation	mm	Measured
	Particle film thickness	mm	Measured
	Ratio of the length of the stationary zone to the cavity circumference	–	Measured

in Ref. [17]. Before starting the experiment, the receiver aperture is enclosed by a rectangular black-painted plate to create a dark room in the cavity so that the contrast between tracers and particles under the light of the lamp is increased.

Previous experiments have shown that the friction between moving particles and the receiver wall is not high enough to ensure an opaque particle film [2,4]. Thus, a wire mesh, shown in Fig. 6(*a*), is welded to the receiver wall to obtain rough surface on the wall. Particles getting stuck between wires form a stationary particle layer on the wall [20]. Stationary particles remain in contact to the wall until the operation ends [21]. They never get exposed to solar rays if the particle film is thick enough but they provide a rough surface for the moving film.

2.2 Optical Elements. In the experiment, two GoPro HERO3+ Silver cameras and two diffusive radiating lamps are employed, shown in Fig. 2. While one camera (② in Fig. 2) is responsible for tracking the white tracers, the other one (③ in Fig. 2) focuses on the circular pin (⑤ in Fig. 2) pressed against the wall. The center of the region of interest of the camera ② is exactly at the mid-level of the receiver's axial length while the axial position of the pin is 40 cm distant to mid-level. The pin is marked with 1 mm-thick black lines as seen in Fig. 5(*a*). In the post-processing, the film thickness is measured by counting the black lines starting from the top. The angle of view of the cameras is 90 deg and 100 deg in horizontal and vertical directions, respectively. The recorded video has a screen resolution of 1920 × 1080 pixels. Finally, the frame rate of the camera is 60 fps.

The lamps are selected based on the homogeneity of the light on the moving particle film, the brightness, the contrast between the tracer and the particle, and the set-up complexity [17]. The distance between the camera and the receiver wall is an important optimization parameter. If it is too small, the picture becomes blurry; if it is too big, then the tracer recognition is badly affected. This distance is optimized as 135 mm by Liebl [17]. Finally, the radial and tangential image distortion resulting from the nature of the camera lens is calibrated by the help of the chessboard image for the optimized distance [17]. Due to the undistortion, the original image is cropped to 1800 × 960 pixels, and 60 pixels from top, bottom, left, and rights are removed. For the given optimized distance and the screen resolution, 1 pixel corresponds to 0.07586 mm, which gives a cropped image size of 136.56 mm × 72.83 mm. The width of the image corresponds to ∼5% of the receiver circumference.

A laser emitting green light is mounted on the stationary black-painted plate enclosing the cavity such that it appears in the camera's ③ field of view in every rotation of the receiver. Thus, by counting image frames after the frame in which the laser spot appears in the camera's field of view the angular position of both cameras can be found in each frame.

2.3 Experiment Design. In this experimental study, two independent and three dependent parameters are utilized. The independent parameters adjusted by the user are receiver rotational speed and particle mass flowrate. Depending on the independent parameters, three dependent parameters which are also the validation parameters for the numerical model are measured. The dependent parameters are the particle film thickness, the axial advance of tracers in one rotation and the ratio of the length of the stationary zone to the cavity circumference. The other parameters like receiver dimension, the type and size of particle and tracers are same for all experiment runs in this study. The dependent parameters are measured for all possible combinations of independent parameters. All the parameters used in experiment are listed in Table 1.

3 Image Processing Routine

The image processing routine of the recorded videos is mainly composed of two steps, namely the tracer recognition and the tracer tracking. As an image processing tool, a script is developed by Liebl [17] in PYTHON by using functions listed in the OpenCV library. The developed approach is similar to 2D PTV. One can calculate the tracer's local velocity based on the camera's frame rate and tracer locations in sequential frames but this is not preferred here because the axial velocity averaged for one rotation is enough for this study. First, the frames are extracted from the recorded video and corrected to eliminate distortion. Then, the center of gravity of each tracer in each frame is determined by the tracer recognition algorithm and stored in a text file. Due to the receiver's rotating imbalance and the misalignment of the assembly structure, carrying cameras and lamps, relative to the receiver centerline, there is a relative motion between the rotating receiver wall and the rotating cameras during the experiment although all the components are fixed to each other well and rotate at the same speed. This relative motion is characterized by the help of the picture of dots glued to the receiver wall, which is seen in Fig. 3. The distance between each dot is 5 mm in both horizontal and vertical directions. The x- and y-coordinates of the pixels containing the center of gravity of each white point in the image are stored in each frame during 100 rotations. It is found that each white point deviates from its mean value such that the shape of the deviation versus frame number curve is sinusoidal. Thus, a sinusoidal curve, showing how much a single white point deviates from its mean value in a specified frame, is fitted with $R^2 > 0.97$ by averaging the results of 100 turns, as seen in Fig. 4. Then, to correct the tracers' position, the below procedure is followed for each tracer.

- The four-corner calibration points closest to the tracer's position are determined.
- By using the frame number, the angular position of the camera is determined. Then, the corresponding amount of the

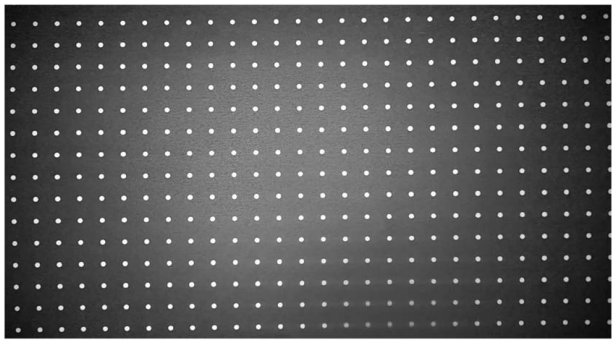

Fig. 3 The picture of dots used for the characterization of the motion between the receiver wall and the camera

deviations in four corner calibration points is determined by using the angular position and sinusoidal fit of each point.

- The deviation at the tracer's position is interpolated by employing the 2D spline interpolation function scipy.interpolate.griddata in PYTHON.
- This procedure is repeated for each tracer, and the resulting position matrix is stored in a text file for each frame.

The approach discussed above is evaluated and the error resulting from using sinusoidal curves in characterization is found as ~1 pixel, corresponding 0.076 mm. Considering the fact that the tracer mean sieve diameter is around 0.983 mm, this error can be assumed as very small.

Finally, the corrected tracer's positions are used by the tracking algorithm and particle trajectories are found by connecting the tracer's position in each frame. The details of the recognition and tracking algorithms are discussed in the following sections.

3.1 Tracer Recognition. To distinguish tracers from ceramic particles, a deterministic approach is followed. The procedure consists of two parts namely, segmentation and filtering. In segmentation part, the RGB pixel value of each pixel in the frame is determined and converted to Hue, Saturation, Value (HSV) value. A sensitivity parameter used in the determination of the upper and the lower bound of the HSV pixel value is defined such that it varies between 0 (only pure white is considered as tracer) and 100 (no segmentation). In the pre-tests, it is observed that if the sensitivity parameter is set as <30 then the tracers located near the edge of the image are not captured because of the bad illumination relative to the center. However, if it is set as >70, some reddish-brown ceramic particles located around the center of the image are detected as tracer due to relatively high illumination at the center. Thus, there is a compromise between tracers located at the center and edges. Tracers located at the center are preferred to the ones at the edges because the ones at the center likely appear again in the next frame while the ones at the edge may disappear. Thus, the sensitivity parameter is set to 30, so the regions higher than HSV value of 225 are considered as tracer candidate. Note that pure white corresponds to a HSV value of 255.

In the filtering step, the detected potential tracers are quantified according to their area, circularity, and aspect ratio. A threshold value for each criterion is defined and only candidates fulfilling the predefined criterion are accepted as the tracer. First, the pixels whose HSV value is in the predefined range (>225) are determined, and the area of the region composed of those neighboring pixels is calculated. Note that the sieve diameter of a tracer is measured as 0.987 mm, meaning that particle diameter-to-pixel length ratio is ~13. In the pre-tests, the range of pixel area, in which a single tracer likely exists, is optimized as 50 to 200 pixel^2 by trial and error. This is because sometimes a part of tracer is eclipsed by a particle and the only the non-eclipsed part is visible. Thus, in order to not lose the track, the lower bound for the area criterion is optimized as 50 pixel^2, which is far below 169 pixel^2. Similarly, in order to prevent to recognize two or more adjoining tracers as a single one, an upper bound is defined. Second, a threshold value of 0.3 for the circularity of the detected region is defined as minimum. Finally, the minimum aspect ratio which is the ratio of the thinnest to widest length within the detected region is defined as 0.01. Figure 5 shows the undistorted and the filtered images. The

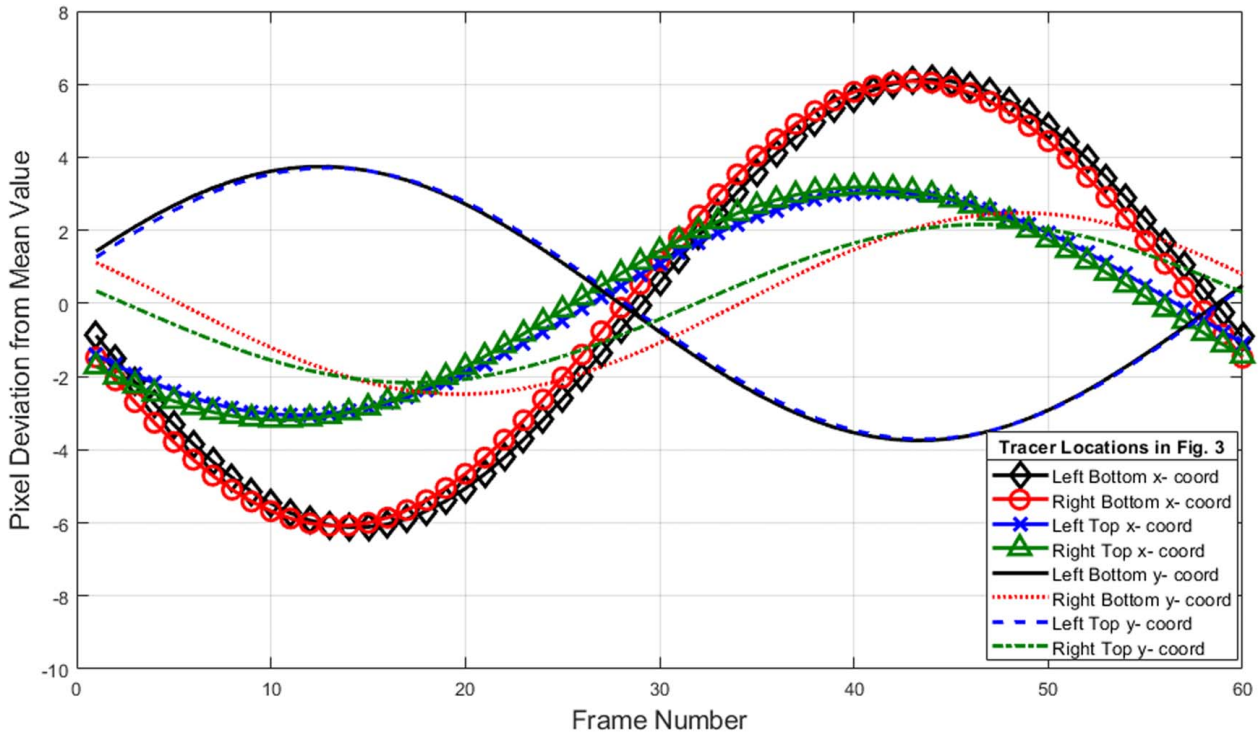

Fig. 4 Pixel deviation from the mean value in one rotation for each tracer point at the corners of the picture of dots based on parameters listed in Table 1

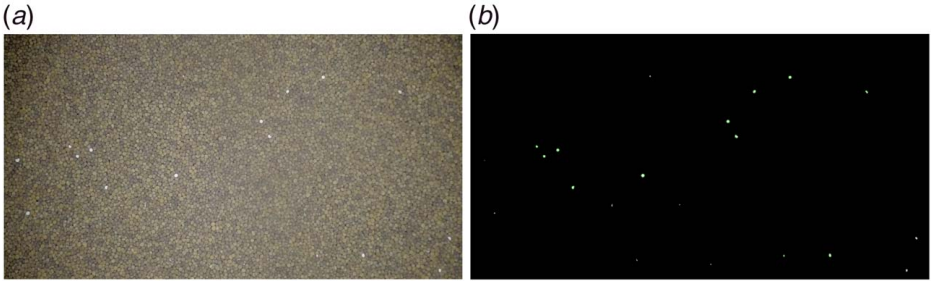

Fig. 5 (*a*) The undistorted image and (*b*) the segmentated and filtered image

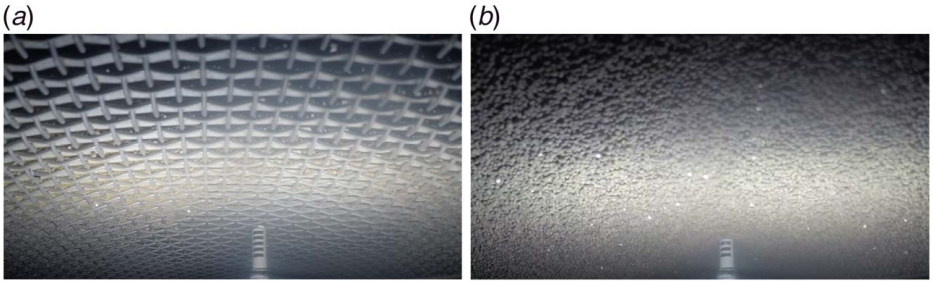

Fig. 6 The pin pressed against the receiver wall (*a*) in empty receiver and (*b*) during experiment

circles in Fig. 5 represent the tracer candidates fulfilling all conditions. Note that criteria thresholds for all parameters are empirical and found by trial and error. During the image processing, the user may adjust these threshold values manually to improve tracking resolution. It is strongly recommended to select original and filtered images randomly often and compare them. The detected regions fulfilling all abovementioned criteria are regarded as "tracer," and the center of gravity of the region is saved in a text file to be used in tracking algorithm later.

3.2 Tracer Tracking. In order to determine the trajectory of tracers, a particle tracking algorithm called 4BestEstimate is integrated to the image processing code [18]. In this approach, the decision of which tracers will be appended to the tracking matrix is made by evaluating four frames, namely the previous two frames, the current frame and the next frame. A search radius where the potential position of the tracer detected in the current frame may be found in the next frame within, is defined by the user. This user-defined parameter should be adjusted carefully such that it is not smaller than the advance of the tracer between two consecutive frames. Setting this parameter very high increases the computational burden because then more candidate tracers are to be checked. Basically, the tracking procedure for tracers is as follows:

(1) In the first frame of the video, all the tracers found in Frame 1 are saved into the tracking matrix. Each row of the matrix represents a track of a new tracer.
(2) The candidate tracers in Frame 2 within the search radius are listed, and the one being closest to the positions in Frame 1 is appended to the tracking matrix. If there is no candidate tracer, the track is finished. It is because tracers may sink into deeper layers due to mixing. Similarly, if a new tracer appears in Frame 2, a new track starts.
(3) For the found couples, a 2D velocity vector with x and y components is calculated as stated in Eq. (1), where v, x, and t are velocity, position, and time. If a new track starts here, it is appended to a new row of the tracking matrix. For those particles, the algorithm starts from *Step 2*.

$$v_n = \frac{x_n - x_{n-1}}{dt} \tag{1}$$

(4) Based on the velocity calculated in *Step 3*, the position of the tracer is estimated in the Frame 3. Then, the search radius is applied around the estimated position. Possible position triplets are determined based on first three frames.
(5) The velocity and acceleration are calculated by using Eqs. (1) and (2) respectively. v_n is calculated by using Frame 2 and Frame 3 while v_{n-1} is found by using Frame 1 and Frame 2.

$$a_n = \frac{v_n - v_{n-1}}{dt} \tag{2}$$

(6) The position of the potential candidates in Frame 4 for detected potential location triplets in step 5 is estimated by using the Eq. (3) [14]

$$x_{n+2} = x_n + 2v_n dt + a_n(2dt)^2 \tag{3}$$

(7) The quartets of which the first two elements are certain and the last two elements are candidates are determined by using the search radius around the potential position found in *Step 6*. If a new tracer appears in this step, a new track starts from *Step 2*.
(8) The found couples from Frame 2 and Frame 3 are appended to the tracking matrix if and only if a track continues in Frame 4. If 2 or more potential quartets fulfill this condition, then the one which has minimum distance between the positions in Frame 3 and Frame 4 is preferred.
(9) The procedure repeats starting from step 2 for the next frame. In each iteration, only the position from Frame 3 is appended to the tracking matrix. The potential tracer in Frame 4 is only used for selection of the triplets Frames 1–3.

It should be noted that if track is lost in any step then it is terminated instead of searching the potential candidates in the future steps. Especially in the moving zone, particles may sink into the non-visible part of the film and reappear in the next frame.

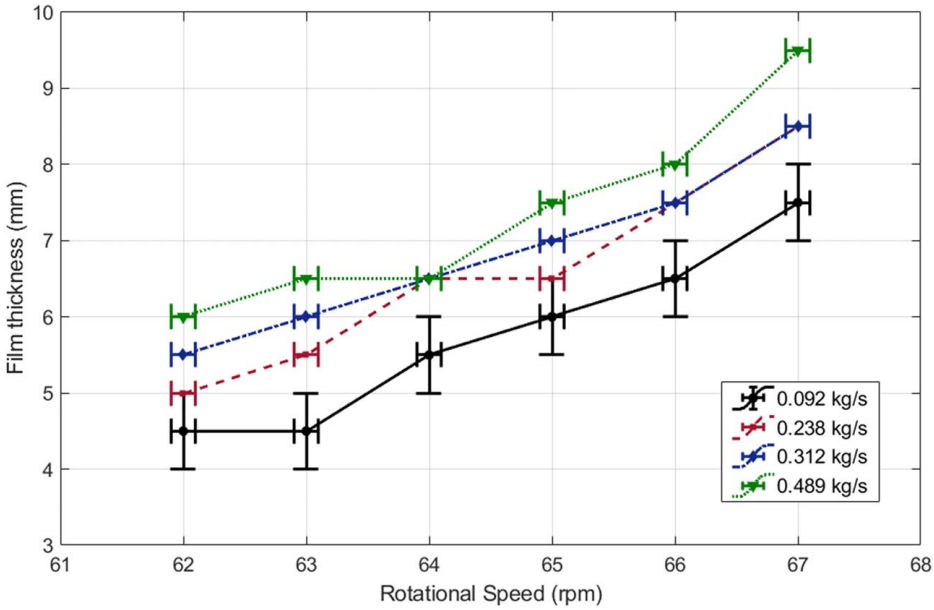

Fig. 7 The film thickness for various mass flowrates and rotational speeds based on parameters listed in Table 1. The vertical error bar corresponds the uncertainty of the measurement technique and same for all measurement points (±0.5 mm). It is only shown for the mass flowrate of 0.092 kg/s to provide legibility. The horizontal error bar shows the measurement uncertainty of the device measuring the rotational speed.

Considering that there might be closely moving tracers in the image, further tracking for sinking-reappearing tracers is not preferred in this study to be on the safe side because it is very hard to estimate if the same tracer is the reappearing one or not. A more detailed explanation about the tracking algorithm and the code can be found in Refs. [17,18].

4 Results and Discussion

As discussed in Sec. 2.3, the experiments are run for all combinations of 6 different rotational speeds and 4 different particle mass flowrates. It is observed that reducing the rotational speed to below 62 rpm causes particles to move in the cavity freely due to insufficient centrifugal forces especially for high flowrates (>0.48 kg/s). Moreover, rotating the receiver at a speed of more than 67 rpm causes that increasing friction force prevents particle motion. The opening between the particle distributor and the receiver wall, as may be seen in Fig. 1(*b*), is ∼1 cm, so as the rotational speed and the flowrate increases, the opening may be clogged. That is why the particle mass flowrate is limited to ∼0.5 kg/s in this experiment. Finally, as rotational speed and flowrate decreases, the welded wire mesh becomes visible, indicating that the thickness of the particle film is small. Thus, six rotational speeds (62, 63, 64, 65, 66, and 67 rpm) and 4 mass flowrates (0.092, 0.218, 0.312, 0.489 kg/s) are investigated to cover the operational range of the CentRec. The videos are recorded for 5 min for each measurement point.

In Fig. 6, the marked pin in the empty and filled receiver is shown. Note that the thickness of black lines and the distance between them is equal to each other and 1 mm. Thus, one can count the black lines to find the film thickness. Figure 7 presents the film thickness for the investigated operational parameters. It can be stated that the film thickness increases with the rotational speed and the particle mass flowrate. As rotational speed increases, the friction between particles forming the particle film increases; thus, the axial velocity profile in the radial direction gets less steep. Note that the values presented in Fig. 7 have an uncertainty of ±0.5 mm. It is because one can say only with naked eye whether a cap of a sphere (particle) is located between two lines on the pin. A more sophisticated code can also detect the exact position of the tip of the spherical cap as suggested by Liebl [17]. In this study, the film thickness is defined as the distance between the tip of topmost particle and the receiver wall. However, due to the dynamic nature of the particle film, some particles may sit slightly higher than the others, thus the film thickness is not constant throughout the receiver circumference but has an uncertainty of one particle radius. Here, it is assumed that there is no pile formation in any part of the particle film due to centrifugal and gravity forces. That's why a more detailed code is not considered here but the measurement is made with naked eye by watching the recorded images and a large uncertainty is assumed, which is half of the distance between two lines on the pin. For example, the film thickness for rotational speed of 67 rpm and mass flowrate of 0.489 kg/s varies between 9 and 10 mm because the spherical cap of topmost particles is always observed in between ninth and tenth lines from the pin tip. Due to the fact that the gap between particle distributor and receiver wall is 10 mm, there may be clogging effect for these operational parameters, which may eventually make that result erroneous. Another point to be emphasized here is that the wire mesh welded to the receiver wall has a diameter of 1 mm which result in a total wire thickness varying between 1 and 2 mm due to assembling technique shown in Fig. 6(*a*). Thus, there is a stationary particle layer that gets entrapped in the wire mesh. The pre-tests have shown that this layer consist of not more than 1 particle in the radial direction.

Due to the opaque nature of particles, only the ones located in the innermost layer of the particle film can be observed. In Fig. 8, the axial advance of these particles in one rotation is presented for various rotational speeds and mass flowrates. From Fig. 8, it can be deduced that the free surface velocity of the film increases with increasing flowrate; in other words, a thicker film yields higher free surface velocity for the same rotational speed. Moreover, the axial advance of particles decreases with increasing rotational speed for the same mass flowrate. The axial advance values for rotational speeds of 62 and 64 rpm and mass flowrate of 0.489 kg/s are not presented here because the trajectory of the particles in one rotation could not be captured with the available image height. The number of tracers detected for each measurement point is also shown in Table 2. A mean standard deviation of

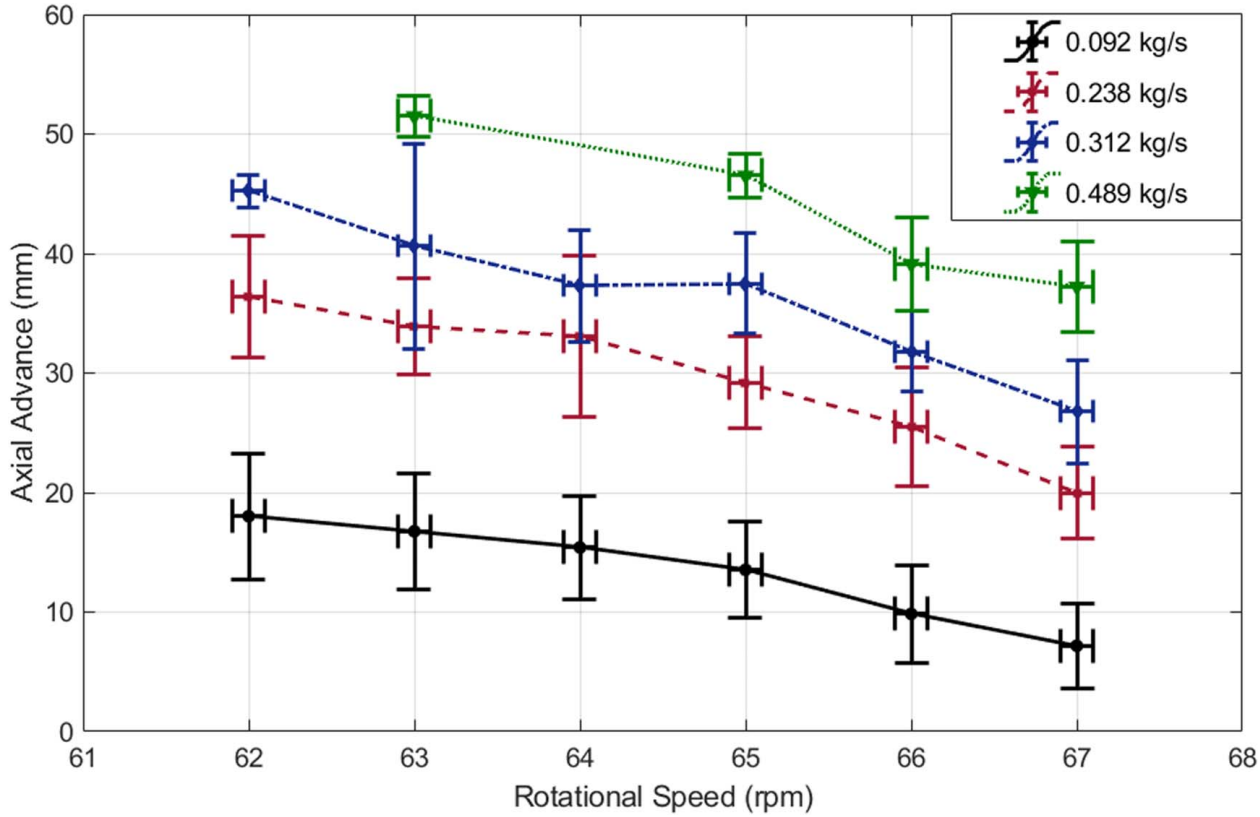

Fig. 8 The axial advance of the tracer in one rotation for various mass flowrates and rotational speeds based on parameters listed in Table 1. The vertical error bar corresponds the mean standard deviation of measurements. The horizontal error bar shows the measurement uncertainty of the device measuring the rotation speed.

measurements is also found for each measurement point and represented as vertical error bar as shown Fig. 8. No relation between the mean standard deviation and operational parameters is observed. For some measurement points, this deviation is relatively small. This is because only a low number of tracers could be tracked, as can be noticed in Table 2, thus the deviation for those measurements should be approached cautiously.

In Fig. 9, the ratio of the length of the stationary zone to receiver circumference is shown for various rotational speeds and mass flowrates. From Fig. 9, it can be observed that this ratio has almost no dependency to rotational speed except for 0.092 kg/s of mass flowrate. In the calculation of this ratio, first, the frames in which the tracer position does not change relative to the previous frame are counted. Then, it is divided to the number of frames corresponding to one receiver rotation. However, it should be noted that the results presented in Fig. 9 are sensitive to the distance criterion chosen to determine if a tracer starts to move in between two consecutive frames. In other words, the ratio changes with the user-defined distance indicating that tracer starts to move if it is exceeded. Thus, this distance is set to 1 mm because the accuracy of pixel deviation correction approach is 1 mm, so the potential noise that may result from this is eliminated. For the same rotational speed, the ratio of the length of the stationary zone to the receiver circumference decreases with increasing flowrate. In other words, as the film gets thicker, the length of the stationary zone gets smaller for the same rotational speed. It proves that the length of the stationary zone is also changing in the radial direction. In other words, a particle's stationarity is changing not only with the angular position but also radial position in the receiver.

Table 2 Number of the detected tracers

	Orifice diameter (mm)	16	22.5	25	30
	Corr. flowrate (kg/s)	0.092	0.238	0.312	0.489
Rotational speed (rpm)	62	135	3	2	–
	63	148	14	7	4
	64	187	15	10	–
	65	171	23	11	2
	66	217	52	23	4
	67	134	31	21	4

One of the challenges in the image processing part is the low number of particles appearing in all frames. Especially in the moving zone, the mixing of the film is very strong; thus, tracers sink into the film, which makes tracking very difficult. In Table 2, the number of tracers tracked for each experiment is tabulated. As can be noticed, the number of tracers is very low for high mass flowrates because the image height is not large enough to capture the tracer's complete axial advance taken in one receiver rotation. In order to increase the accuracy, a track is always started from the stationary zone because starting a track in moving zone would lead to less accuracy in measurement of axial advance and stationary zone ratio due to low camera frame rate.

In the post processing of the recorded videos, there are several potential sources of error. First, there is a reprojection error, defined as the distance between the measured position and the projected position of a point in the image plane. This error is found as 0.0523 pixel for the type of cameras used in this study and given distance between particle film and camera by Liebl [17]. Second, there is an error resulting from the curve fit to characterize pixel deviation. This error is also found to be approximately one pixel in each calibration point. Lastly, there is also an error due to linear interpolation of the particle trajectory between sequential frames. However, in this study, only the axial displacement of particles, which is a path-independent parameter, in one rotation is measured. Thus, the overall optical error is calculated as ~1

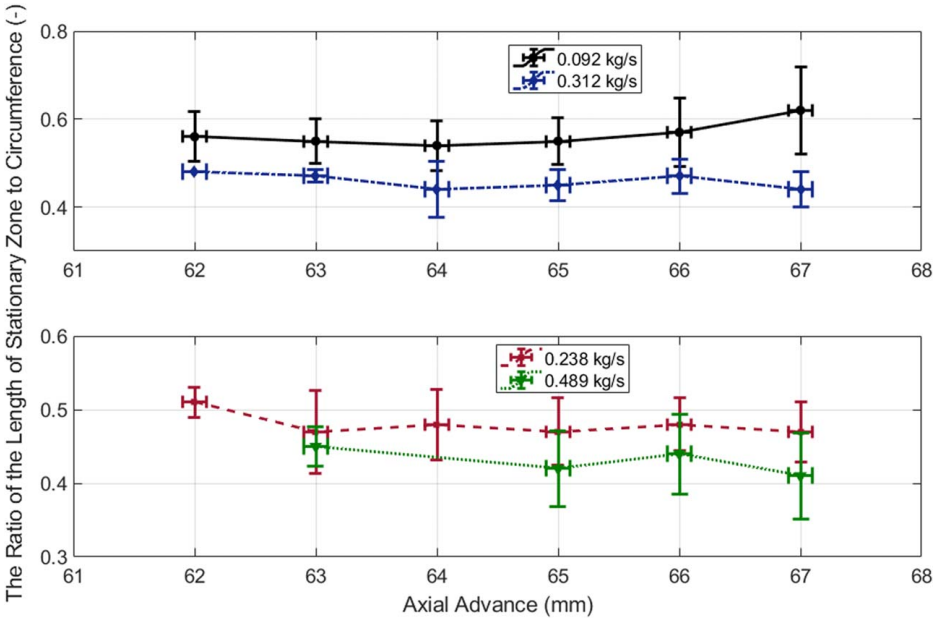

Fig. 9 The ratio of the length of the stationary zone to the cavity circumference for various mass flowrates and rotational speeds based on parameters listed in Table 1. The figure is split to two plots to increase legibility of the figure. The vertical error bar corresponds the mean standard deviation of the measurement points. The horizontal error bar shows the measurement of uncertainty of the device measuring the rotation speed.

pixel, which is negligibly small compared to particle's axial advance in one rotation. There is also a potential error, which is hard to quantify, in the tracer detection algorithm but this is minimized by optimizing the empirical parameters as discussed in Sec. 3.1. If a tracer could not be detected via detection algorithm, then the track is automatically terminated. Moreover, the movement pattern of the all trajectories is checked. If any trajectory does not have the common pattern, i.e., movement in stationary zone or unphysical upward motion in moving zone, it is omitted. This situation is very likely due to that a pixel region is detected as tracer although it is not the case. There may be also the case that one tracer sinks and another one reappears in the location where the first one is supposed to be in the next frame. In order to eliminate this risk, the tracer to particles ratio is kept low (0.01). Thus, the average distance between tracers in a frame is increased. Finally, there may be also an error in the tracking algorithm such that the same tracer is not tracked during its trajectory although all tracers are detected correctly in each frame. However, this situation also causes a different trajectory pattern and can be noticed by the user. For a more robust model, a pattern recognition algorithm can also be employed in the future study. Moreover, using a camera with higher frame rate and 3D tracking technique may reduce the errors in tracking algorithm.

5 Conclusions

In this study, an experimental setup is designed for tracking the trajectory of the particles and the measurement of the film thickness. Experiments were run for six rotational speeds (62, 63, 64, 65, 66, and 67 rpm) and four mass flowrates (0.092, 0.218, 0.312, 0.489 kg/s) for an experiment scale centrifugal solar particle receiver. Then, the raw results are post-processed with an image processing routine based on 4BestEstimate algorithm. The results have shown that the film thickness, the axial advance of particles in one receiver rotation and the ratio of the length of stationary zone to the cavity circumference have been sufficiently characterized and can be used as parameters in the validation of the DEM-based numerical model.

Acknowledgment

This work is supported by DLR—DAAD Research Fellowship Program.

Conflict of Interest

There are no conflicts of interest.

Data Availability Statement

The datasets generated and supporting the findings of this article are obtainable from the corresponding author upon reasonable request. The authors attest that all data for this study are included in the paper. Data provided by a third party listed in Acknowledgment.

Nomenclature

a_n = acceleration of a tracer in a frame
v_n = velocity of a tracer in a frame
x_n = position of a tracer in a frame
dt = time interval between two consecutive frames

References

[1] Ho, C. K., 2016, "A Review of High-Temperature Particle Receivers for Concentrating Solar Power," Appl. Therm. Eng., **109**, pp. 958–969.
[2] Wu, W., 2014, "A Centrifugal Particle Receiver for High-Temperature Solar Applications," Ph.D. thesis, RWTH Aachen University, Aachen, Germany.
[3] Wu, W., Trebing, D., Amsbeck, L., Buck, R., and Pitz-Paal, R., 2015, "Prototype Testing of a Centrifugal Particle Receiver for High-Temperature Concentrating Solar Applications," ASME J. Sol. Energy Eng., **137**(4), p. 041011.
[4] Ebert, M., Amsbeck, L., Jensch, A., Hertel, J., Rheinlaender, J., Trebing, D., Uhlig, R., and Buck, R., 2016, "Upscaling, Manufactuirng and Test of a Centrifugal Particle Receiver," ASME 2016 10th International Conference on Energy Sustainability ES2016, Charlotte, North Carolina, June 26–30, 2016.
[5] Johnson, E. F., 2021, "Advances in Modeling High Temperature Particle Flows in Concentrating Solar Power," Ph.D. thesis, Middle East Technical University, Ankara, Turkey.

[6] Grobbel, J., 2019, "Modeling Solar Particle Receivers With the Discrete Element Method," Ph.D. thesis, RWTH Aachen University, Aachen, Germany.
[7] Grobbel, J., Brendelberger, S., Henninger, M., Sattler, C., and Pitz-Paal, R., 2020, "Calibration of Parameters for DEM Simulations of Solar Particle Receivers by Bulk Experiments and Surrogate Functions," Powder Technol., **364**, pp. 831–844.
[8] Hicdurmaz, S., Johnson, E., Grobbel, J., Amsbeck, L., Buck, R., and Hoffschmidt, B., 2020, "Numerical Heat Transfer Modelling of a Centrifugal Solar Particle Receiver," SolarPACES Virtual Conference, AIP Conference Proceedings (accepted).
[9] Ho, C. K., Christian, J. M., Romano, D., Yellowhair, J., Siegel, N., Savoldi, L., and Zanino, R., 2017, "Characterization of Particle Flow in a Free-Falling Solar Particle Receiver," ASME J. Sol. Energy Eng., **139**(2), p. 021011.
[10] Jesuthasan, N., Baliga, B. R., and Savage, S. B., 2006, "Use of Particle Tracking Velocimetry for Measurements of Granular Flows: Review and Application," KONA Powder Particle J., **24**, pp. 15–26.
[11] Sarno, L., Tai, Y.-C., Carravetta, A., Martino, R., Papa, M. N., and Kuo, C.-Y., 2019, "Challenges and Improvements in Applying a Particle Image Velocimetry (PIV) Approach to Granular Flows," J. Phys.: Conf. Ser., **1249**(1), p. 012011.
[12] Quinnell, J. A., and Davidson, J. H., 2013, "Buoyancy Driven Mass Transfer in a Liquid Desiccant Storage Tank," ASME J. Sol. Energy Eng., **135**(4), p. 041009.
[13] Ozalp, N., Chien, M.-H., and Morrison, G., 2013, "Computational Fluid Dynamics and Particle Image Velocimetry Characterization of a Solar Cyclone Reactor," ASME J. Sol. Energy Eng., **135**(3), p. 031003.
[14] Gollin, D., Brevis, W., Bowman, E., and Shepley, P., 2017, "Performance of PIV and PTV for Granular Flow Measurements," Granular Matter, **19**(42), pp. 1–16.
[15] Heikkila, J., and Silven, O., 1997. "A Four-Step Camera Calibration Procedure With Implicit Image Correction," Proceedings of the IEEE Computer Society Conference on Computer Vision and Pattern Recognition, IEEE, San Juan, PR, June 17–19, pp. 1106–1112,
[16] Weng, J., Cohen, P., and Herniou, M., 1992, "Camera Calibration with Distortion Models and Accuracy Evaluation," IEEE Trans. Pattern Anal. Mach. Intell., **14**(10), pp. 965–980.
[17] Liebl, L., 2020, "Development and Optimization of an Optical System and an Image Processing Code to Investigate the Particles Motion in a Solar Particle Receiver," Master's thesis, Karlshure Institute of Technology, Karlshure, Germany.
[18] Ouellette, N. T., Xu, H., and Bodenschatz, E., 2006, "A Quantitative Study of Three-Dimensional Lagrangian Particle Tracking Algorithms," Experiments Fluids, **40**(2), pp. 301–313.
[19] Franke, A., 2021, "Uebersicht und Auswahl von Technologien zur Messung von Partikelmassenstroemen in Solaren Hochtemperaturreceivern," Bachelor's thesis, Stuttgart University, Stuttgart, Germany.
[20] Ebert, M., Amsbeck, L., Rheinländer, J., Knothe, B. S., Schmitz, S., Sibum, M., Uhlig, R., and Buck, R., 2019, "Operational Experience of a Centrifugal Particle Receiver Prototype," Solar PACES, AIP Conference Proceedings, Casablanca, Morocco, Oct. 1–4, 2019, pp. 1–8, 2126(030018).
[21] Amsbeck, L., Buck, R., Ebert, M., Gobereit, B., Hertel, J., Jensch, A., Rheinländer, J., Trebing, D., and Uhlig, R., 2017, "First Tests of a Centrifugal Particle Receiver with a 1m2 Aperture," SolarPACES, AIP Conference Proceedings, Santiago, Chile, Sept. 26–29, 2017, pp. 1–7, 2033(040004).